
Article:
Morita, T., Sakawa, Y., Kuramitsu, Y. et al. (8 more authors) (2017) Characterization of electrostatic shock in laser-produced optically-thin plasma flows using optical diagnostics. Physics of Plasmas. 072701. pp. 1-8. ISSN 1089-7674

https://doi.org/10.1063/1.4990058

Characterization of electrostatic shock in laser-produced optically-thin plasma flows using optical diagnostics

T. Morita,[1, a)] Y. Sakawa,[2] Y. Kuramitsu,[2, b)] S. Dono,[3] H. Aoki,[4] H. Tanji,[3] J. N. Waugh,[5] C. D. Gregory,[6, c)] M. Koenig,[6] N. C. Woolsey,[5] and H. Takabe[2, d)]

[1)] *Faculty of Engineering Sciences, Kyushu University, 6-1 Kasuga-Koen, Kasuga, Fukuoka 816-8580, Japan*

[2)] *Institute of Laser Engineering, Osaka University, 2-6 Yamada-oka, Suita, Osaka 565-0871, Japan*

[3)] *Graduate School of Engineering, Osaka University, 2-6 Yamada-oka, Suita, Osaka 565-0871, Japan*

[4)] *Graduate School of Science, Osaka University, 1-1 Machikane-yama, Toyonaka, Osaka 560-0043, Japan*

[5)] *Department of Physics, University of York, Heslington, York, YO10 5DD, United Kingdom*

[6)] *LULI, École Polytechnique, CNRS, CEA, UPMC, Route de Saclay, 91128 Palaiseau, France*

We present a method of evaluating the properties of electrostatic shock in laser-produced plasmas by using optical diagnostics. A shock is formed by a collimated jet in counter-streaming plasmas in nearly collisioinless condition, showing the steepening of the transition width in time. In the present experiment, a streaked optical pyrometry was applied to evaluate the electron density and temperatures in the upstream and downstream regions of the shock so that the shock conditions are satisfied, by assuming thermal bremsstrahlung emission in optically thin plasmas. The derived electron densities are nearly consistent with those estimated from interferometry.

PACS numbers: 52.50.Jm, 52.35.Tc, 52.70.Kz

I. INTRODUCTION

Collisionless shocks have been widely studied in various research fields in the universe, space, and laboratory plasmas because of their importance as the origin of particle acceleration. In astrophysical context, for example, x-ray emissions from accelerated electrons have been observed from supernova remnant shocks[1–3], and particle accelerations have been directly detected by satellites in space plasmas[4,5].

Collisionless shocks can be simply classified with respect to the electromagnetic properties[6]: laminar electrostatic (ES) shock and turbulent electromagnetic (EM) shock. ES shocks are rare in space and astrophysical plasmas because most of the plasmas are magnetized. They, however, exist in specific conditions such as auroral zone in planets[7–9] and solar corona[10] even in magnetized plasmas along the magnetic field one-dimensionally, and can accelerate charged particles rapidly with ES potentials. Also, ES shock can be formed in an early stage of EM shock formation as suggested by a particle-in-cell simulation[11]. On the other hand, most shocks in the universe or space are magnetized shocks in which magnetic field plays important role in the shock formation. EM shock can be formed in anisotropic collisionless plasma, for example, in counter-streaming plasmas via Weibel instability. Recent numerical works have indicated that EM shocks can be formed in weak magnetic field or without magnetic field in relativistic[12–14] and even in non-relativistic[11,15–17] counter-streaming plasmas.

Laboratory experiments can be scaled to the astrophysical phenomena in collisionless plasmas considering the dimensionless parameters[18] and can be alternative ways to investigate astrophysical high-energy phenomena. Collisionless shocks have been investigated with high-power laser systems because high-power laser irradiation on a solid target generates high-speed counter-streaming plasmas[19] and their interaction can be collisionless[20]. ES Shocks have been generated in laser-produced counter-streaming plasmas and measured with optical diagnostics: shadowgraphy[21,22], interferometry[21,23], self-emission streaked optical pyrometry (SOP)[24], and proton radiography[25,26]. In addition, experiments for EM shocks have been recently proposed and studied with large laser systems[27,28] such as Omega and National Ignition Facility (NIF). Collisionless counter-streaming plasmas have been measured with laser Thomson scattering technique[29,30] and the magnetic field structures induced by Weibel instability have been observed by proton radiography[31,32] as an early stage of EM shock formation.

Laser Thomson scattering technique enable us to de-

[a)] Electronic mail: morita@aees.kyushu-u.ac.jp

[b)] Present address: Department of Physics, National Central University, No. 300, Zhongda Rd., Zhongli District, Taoyuan City 32001, Taiwan

[c)] Present address: Central Laser Facility, Rutherford Appleton Laboratory, Harwell Campus, Didcot OX11 0QX, United Kingdom

[d)] Present address: Helmholtz-Zentrum Dresden-Rossendrof, Bautzner Landstrasse 400, 01328 Dresden, Germany

rive local plasma parameters such as density, temperature, and drift velocity, as well as the Mach-number of a shock[33]. This is, however, limited in local measurements and therefore, requires simultaneous measurements to obtain global structures such as gated optical imager, interferometry, and SOP[33]. SOP has been widely applied to optically thick plasmas in inertial confinement fusion experiments and high-energy-density experiments[34,35] to measure the plasma temperature. Such plasmas can be regarded as a blackbody radiator, and $T_\mathrm{b} \sim T_\mathrm{e} \sim T_\mathrm{i}$, where T_e and T_i are, respectively, electron and ion temperatures, and T_b is brightness temperature derived assuming blackbody radiation at a certain wavelength. In this case, the emission from the plasma directly connected to the plasma temperature. On the other hand, in an optically thin plasma, T_e is much larger than T_b, and the emission is expressed as thermal bremsstrahlung emission. In the present experiment, the plasmas created by a high-power laser system were mainly optically thin. Nevertheless, the measurement of emission in optically thin plasma is useful because it depends on both the electron density and temperature, and a sudden emission change shows the plasma density and/or temperature jump. Bremsstrahlung emission in optically thin plasmas depends on electron density squared but only the inverse square root of electron temperature[36], meaning the inference of electron temperature from SOP is challenging.

In this paper, we propose a method to evaluate the electron temperatures and densities in the upstream and downstream regions of an ES shock in optically thin laser-produced plasmas by using SOP. The experimental conditions for the generation of the counter-streaming plasmas are given in Ref. 37. A shock is observed only in the counter-streaming plasmas, and no shock is observed without a counter flow, indicating that the counter-streaming interaction is essential for shock formation. Here, the emission jump at the shock surface is quantitatively investigated combined with the jump conditions of a shock to obtain the plasma densities and temperatures in the upstream and downstream regions. The derived density is nearly consistent with that obtained from interferometry. Unlike our previous work on the local measurement at a shock[33], the proposed analysis technique measures the electron temperature and density as well as the global structure of a shock. Though this technique is applied to an ES shock in this paper, it is applicable to any shocks satisfying the jump conditions formed in optically thin plasmas, including an EM shock which is expected to be generated in near future with NIF laser facility[38].

II. EXPERIMENT

The experiment was performed with Gekko-XII (GXII) HIPER laser system at Institute of Laser Engineering, Osaka University: frequency tripled Nd:Glass laser (351 nm) which has the energy of $\sim$ 120 J/beam in 500 ps pulse duration. The focal spot diameter was 300 μm, and four laser beams were focused on a surface of target with separations of 100–250 μm. As discussed in Ref. 37, this beam spot separation forms a confined jet-like plasma structure on the axis.

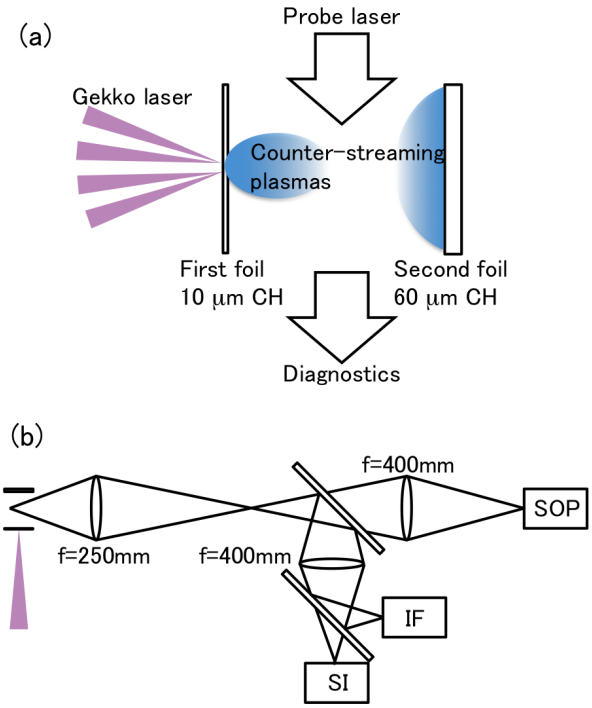

FIG. 1. (color online) (a) A schematic view of the experimental setup and the double-foil target. (b) A top view of the optical diagnostics. The interference image is measured by IF and SI, and the self-emission was measured by SOP.

We used two types of targets: One is a double-foil target consisting of two CH foils with the thicknesses of 10 μm and 60 μm, and the other is a single-foil target with a 10 μm thick foil. Figure 1(a) shows the schematic view of the double-foil target. Four laser beams were focused on the 10 μm thick foil (first foil) and plasma flow was created at the rear-side of the first foil. The second foil was ablated by the radiation early in time and by the first foil plasma later in time. As a result, counter-streaming plasmas were created between the two foils. The single-foil target has only the first foil, and no counter-flow was generated.

Plasma expansion and shock formation were observed from the transverse to the plasma expanding direction. Self-emission was measured by SOP with an interference filter which has the central wavelength of 450 nm. The linearity in time, uniformity in space, and sensitivity of the streak camera for SOP were calibrated to derive the emission energy from the digital counts in each pixel[39]. The electron density and the phase difference were measured by Nomarski interferometry (IF) and streaked interferometry (SI) with a probe laser: a frequency doubled

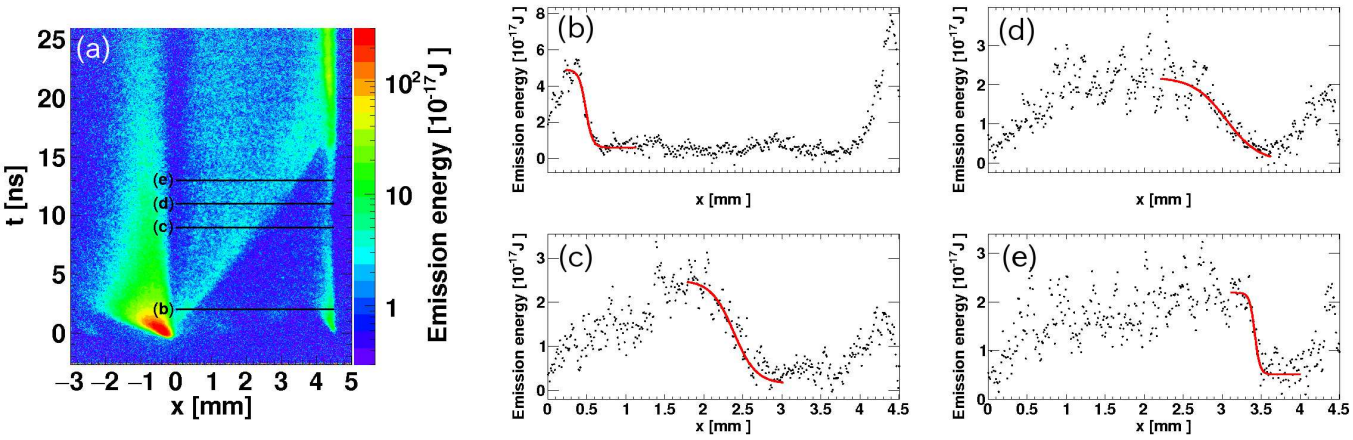

FIG. 2. (color online) (a) The temporal variation of the emission energy for the double-foil target obtained by SOP. The first and second foils are at $t = 0$ and 4.5 mm, respectively. The profiles of the emission energy obtained at (b) $t = 2.0$, (c) 9.0, (d) 11, and (e) 13 ns. Solid lines in (b)–(e) are the fitted lines with Eq. (1).

Nd:YAG laser (532 nm) with a pulse width of $\sim$ 14 ns. The electron density profile was calculated from IF, and the time variation of the one-dimensional density was estimated from SI. IF image was recorded by an intensified charge coupled device (ICCD) camera with a gate width of 250 ps.

III. RESULTS AND DISCUSSION

A. Shock observation

Figure 2(a) shows the temporal variation of the emission energy for the double-foil target obtained by SOP. The surfaces of two foils are at $x = 0$ and 4.5 mm, and $t = 0$ ns corresponds to the laser timing. The plasma created at the first foil ($x = 0$ mm) by the laser beams begins to propagate at $t = 0$ ns, and reaches the second foil ($x = 4.5$ mm) at $t \sim 15$ ns. After that, the second foil is ablated and heated by the plasma from the first foil[40]. The second foil is also ablated and plasma is created by the radiation from the first foil at the laser timing[19,37]. Figures 2(b), 2(c),2(d), and 2(e) show the profiles of the emission energy at $t = 2.0$, 9.0, 11, and 13 ns, respectively. The emission energies suddenly change at $x \simeq 0.5$ mm in Fig. 2(b), $x \simeq 2.3$ mm in Fig. 2(c), $x \simeq 3$ mm in Fig. 2(d), and $x \simeq 3.5$ mm in Fig. 2(e). In order to evaluate the transition width of the emission energy ϵ, the profiles are fitted with the following equation:

$$\epsilon(x) = a + b\tanh(-\frac{x - x_{\rm s}}{W}), \qquad (1)$$

where a, b, W, and $x_{\rm s}$ are fitting parameters, and the fitted functions are plotted in Figs. 2(b)–2(e). The parameters W and $x_{\rm s}$ represent the width and position of the transition, respectively.

Figure 3(a) shows the temporal variation of the emission energy for the single-foil target. The laser beams irradiates the foil at $x = 0$ mm from the negative x direction, and the plasma is created and expands along the laser axis. Figures 3(b) and 3(c) show the emission energy profiles at $t = 2.0$ and 7.4 ns, respectively. The emission energy profiles are fitted with Eq. (1) as shown with the solid lines.

Figure 4(a) shows the temporal variations of W derived for double and single-foils from Figs. 2(a) and 3(a), respectively. Comparing the results for the double-foil and single-foil targets, the velocity of the plasmas from the first foil for the double-foil target is less than that for the single-foil target. Furthermore, the transition width W for the double-foil target is shorter than that for the single-foil target. These two effects might be caused by the existence of the counter-streaming flows in the double-foil target. Unlike the double-foil target case, W increases monotonically for the single-foil target, meaning no shock is formed in expanding plasmas in vacuum. In the double-foil experiment, the transition width gradually increases to wider than 0.2 mm until $t \sim 10$ ns, then starts to decrease to shorter than 0.1 mm at $t > 12$ ns. This shortening in the transition width indicates the shock formation. A clear shock is created at $t > 12$ ns, and propagates toward the second foil. The emission distribution shows that the upstream and downstream regions correspond to right and left regions, respectively [upstream at $x > 3.5$ mm and downstream at $x < 3.5$ mm in Fig. 2(e)], and the upstream flow comes from the second foil as shown in Fig. 2(a) at $t \gtrsim 0$ ns and $x \sim 4.5$ mm. The shock velocity $v_{\rm s}$ is almost constant and evaluated by a linear fitting as $v_{\rm s} = 220 \pm 8$ km/s as shown with a solid line in Fig. 4(b). $v_{\rm s}$ is slower than initial expansion velocity as indicated by a dashed line ($v_{\rm s}$) which is extended from a solid line, as a result of counter-streaming interaction.

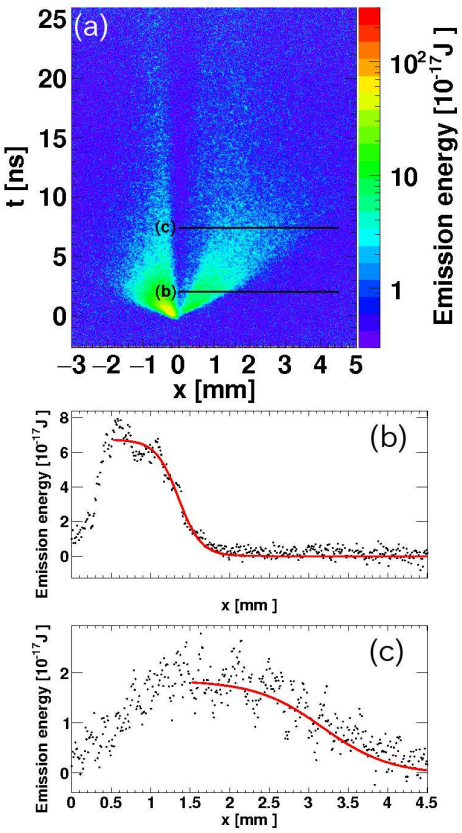

FIG. 3. (color online) (a) The emission energy of the single-foil target obtained by SOP. The profiles of the emission energy obtained at (b) $t = 2.0$, (c) 7.4 ns after laser pulses, respectively. Solid lines in (b) and (c) are the fitted lines with Eq. (1).

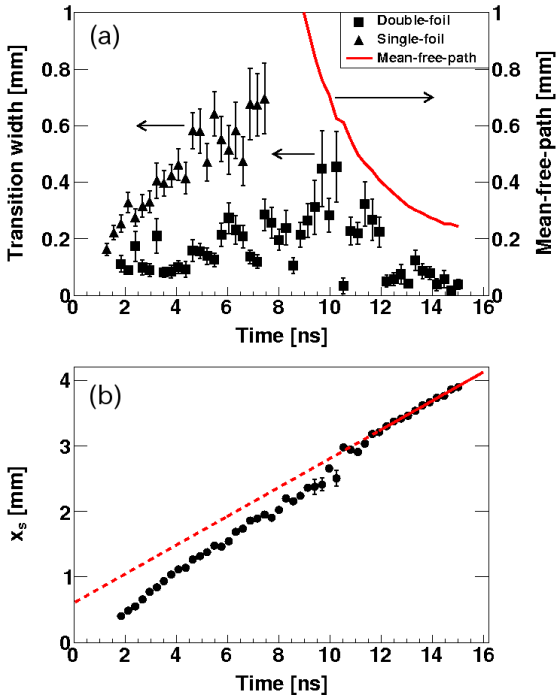

FIG. 4. (color online) (a) The temporal evolution of the evaluated transition width W for double (closed-squares) and single (closed-rectangles) foils. The solid line shows the calculated ion-ion mean-free-path (λ_{ii}) assuming the electron density $n_e \sim 1.7 \times 10^{19}$ cm^{-3}. (b) The positions of transition x_s evaluated by fitting the emission energy profiles for double-foil data with Eq. (1). A linear fitting at $t > 12$ ns is also shown with a solid line. The shock velocity is evaluated as 220 ± 8 km/s.

B. Estimation of electron temperature at the vicinity of a shock

Here, we estimate the plasma densities and temperatures in the upstream and downstream regions of the shock. The plasmas were obviously optically thin at the time ($t \simeq$12–15 ns) and the position ($x \simeq$3–4 mm) where the shock was generated, because the probe laser could penetrate them and was detected with IF and SI as shown in Figs. 7(a) and 8(a). Radiation energy density from such plasmas is expressed with thermal bremsstrahlung emission[41] as

$$\epsilon_\lambda(T_e) = \frac{2^5\pi e^6}{(4\pi\epsilon_0)^3 3mc^2\lambda^2}\left(\frac{2\pi}{3m}\right)^{1/2} g^{ff} \times \frac{Z^2 n_e n_i}{\sqrt{T_e}} \exp(-hc/\lambda T_e) \quad (2)$$

$$\propto Z^3 n_i^2 \exp(-hc/\lambda T_e) g^{ff}/\sqrt{T_e}, \quad (3)$$

where e is the elementary charge, ϵ_0 is the permittivity of free space, c is the speed of light, m is the electron mass, $\lambda \simeq 450$ nm is the wavelength, h is the Planck constant, Z is the degree of ionization, and g^{ff} is a velocity averaged

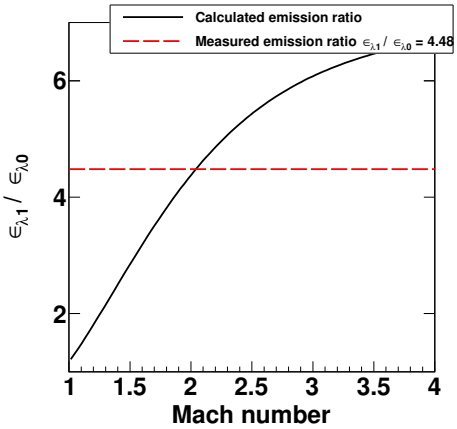

FIG. 5. (color online) The emission ratio calculated from Eq. (4) as a function of an upstream Mach-number M using Eqs. (5), (6), and (7) and $g_1^{ff}/g_0^{ff} = 1.17$ at the shock position of $x = 3.5$ mm at $t = 13$ ns. The measured emission ratio of $\epsilon_{\lambda 1}/\epsilon_{\lambda 0} \simeq 4.48$ is shown with dashed line.

Gaunt factor[42]. The ratio of ϵ_λ in the downstream to upstream regions is calculated as

$$\frac{\epsilon_{\lambda 1}}{\epsilon_{\lambda 0}} = \left(\frac{n_1}{n_0}\right)^2 \left(\frac{T_1}{T_0}\right)^{-1/2} \left(\frac{g_1^{ff}}{g_0^{ff}}\right) \times \exp\left[-\frac{hc}{\lambda T_0}\left(\left(\frac{T_1}{T_0}\right)^{-1} - 1\right)\right], \quad (4)$$

where T_0 and T_1 are the electron temperatures at the upstream and downstream, respectively. On the other hand, from the shock condition, temperature and density ratios in a perfect gas are expressed with an upstream Mach-number $M = v_0/c_{s0}$,

$$\frac{T_1}{T_0} = \frac{[2\gamma M^2 - (\gamma-1)][(\gamma-1)M^2+2]}{(\gamma+1)^2 M^2}, \quad (5)$$

$$\frac{n_1}{n_0} = \frac{v_0}{v_1} = \frac{(\gamma+1)M^2}{(\gamma-1)M^2+2}, \quad (6)$$

where v_0 and v_1 are, respectively, the upstream and downstream flow velocities in the shock rest frame, c_{s0} is the upstream sound velocity, and γ is the adiabatic constant. Here, v_0 is calculated from $v_0 = u_2 + v_s$, where $v_s = 220$ km/s as shown in Fig. 4(b) and $u_2 = (4.5\text{ mm} - x_s)/t$ for given time t and shock position x_s. In the upstream region, c_{s0} is expressed as $c_{s0} = \sqrt{(Z+\gamma)T_0/m_i}$, where m_i is the ion mass, and we assume $T_0 = T_e = T_i$, electrons are isothermal, $\gamma = 5/3$, and $Z = 3.5$. Therefore, T_0 is expressed as a function of M, t, and x_s as

$$T_0 = \frac{m_i}{(Z+\gamma)M^2}\left(v_s + \frac{4.5\text{ [mm]} - x_s}{t}\right)^2. \quad (7)$$

Substituting Eqs. (5), (6), and (7) into Eq. (4), the ratio $\epsilon_{\lambda 1}/\epsilon_{\lambda 0}$ is expressed as a function of M, t, x_s, and g_1^{ff}/g_0^{ff}.

At $t = 13$ ns, for example, $x_s = 3.5$ mm [see Figs. 2(e) and 4(b)], and hence, $\epsilon_{\lambda 1}/\epsilon_{\lambda 0}$ is expressed as shown in Fig. 5 using the Gaunt factor ratio $g_1^{ff}/g_0^{ff} = 1.17$. Considering the measured emission ratio of $\epsilon_{\lambda 1}/\epsilon_{\lambda 0} \simeq 4.48$ [Fig. 2(e)], the Mach-number is derived as $M \simeq 2.0$. Applying $M = 2.0$ in Eqs. (5), (6), and (7), we obtain $T_0 \simeq 43$ eV, $T_1 \simeq 92$ eV, and $n_1/n_0 \simeq 2.3$.

For a given T_e, the emission energies for the bremsstrahlung emission are expressed as a function of n_e. Figure 6 shows the emission energies calculated with Eq. (2) in the upstream ($T_e = T_0 \simeq 43$ eV) and the downstream ($T_e = T_1 \simeq 92$ eV) regions. The Gaunt factors are evaluated using the above temperatures as[42] $g_0^{ff} \sim 1.8$ and $g_1^{ff} \sim 2.1$, and the ratio $g_1^{ff}/g_0^{ff} \sim 1.2$ is consistent with that used in the calculation of $\epsilon_{\lambda 1}/\epsilon_{\lambda 0}$ shown in Fig. 5. The measured emission energies in the upstream $\epsilon_{\lambda 0} = 5.04 \times 10^{-18}$ J (dotted line) and downstream $\epsilon_{\lambda 1} = 2.26 \times 10^{-17}$ J (dash-dot line) at $t = 13$ ns [Fig. 2(e)] are also shown in Fig. 6. The positions of intersections shown with arrows give the electron densities $n_0 \simeq 7.4 \times 10^{18}$ cm^{-3} in the upstream region and $n_1 \simeq 1.7 \times 10^{19}$ cm^{-3} in the downstream region.

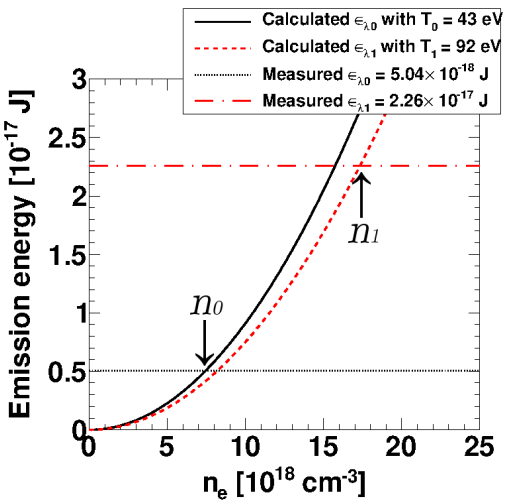

FIG. 6. (color online) The calculated thermal bremsstrahlung emission energies in the upstream ($T_0 \simeq 43$ eV: solid line) and the downstream ($T_1 \simeq 92$ eV: dashed line) region at $t = 13$ ns and $x = 3.5$ mm using Eq. (2). The measured emission energy at $t = 13$ ns in the upstream ($\epsilon_{\lambda 0} \simeq 5.04 \times 10^{-18}$ J: dotted line) and downstream ($\epsilon_{\lambda 1} \simeq 2.26 \times 10^{-17}$ J: dash-dot line) regions are also shown.

C. Electron density from interferometry

Electron density was evaluated by using IF and SI simultaneously with same experimental conditions as SOP measurements but in different laser shot. IF shows complicated fringe structures later in time ($t \gtrsim 10$ ns) and it is impossible to calculate n_e from IF. Here, we evaluate the validity of estimating electron density from one-dimensional interferogram of SI early in time comparing with IF, and estimate the electron density later in time only from SI.

Figure 7(a) shows the IF data at $t = 5$ ns for the double-foil target. The interference fringes lie in the horizontal direction without plasmas and shift upward as the plasma density increases. The first and second foils are located at $x = 0$ and 4.5 mm, respectively, as shown with dashed lines. The laser beams are focused at $x = 0$ mm and $y \sim 2.6$ mm (dash-dot line). The electron density n_e on the axis ($y = 2.6$ mm) of the expanding plasma is calculated with numerical Abel inversion method from the lower region ($y < 2.6$ mm), and shown in Figs. 7(b) with the solid line. The interferogram is not axisymmetric especially in upper half ($y > 2.6$ mm) because of high-density plasma near the second foil ($x \sim$3–4 mm and $y \sim$3–5) coming from the supporting frame. In the regions $x < 2.5$ mm and $x > 4.1$ mm, the interference fringes disappear since the electron density is too high or the plasma size is too large, and the probe laser is not detected in the optical diagnostics. The maximum calculable electron density is less than $\sim 2 \times 10^{19}$ cm^{-3}. The electron density at $x = 3.5$ mm is about 3×10^{18} cm^{-3}

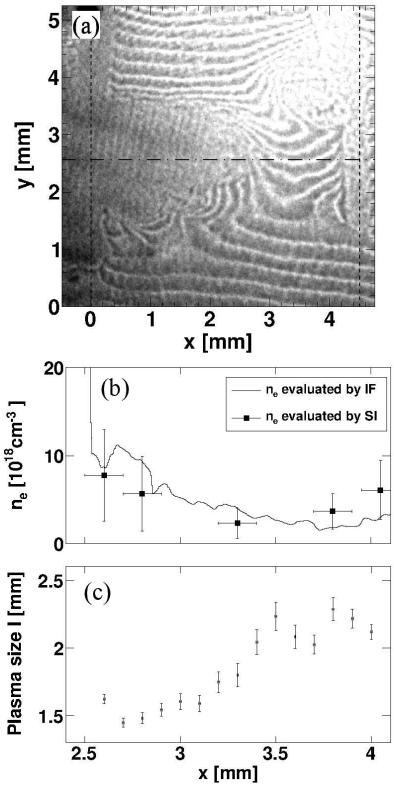

FIG. 7. (a) IF data obtained at $t = 5$ ns for the double-foil target. The first and second foils are located at $x = 0$ and 4.5 mm, respectively, as shown with dashed lines. (b) Electron density n_e profile at $y = 2.6$ mm obtained by IF (solid line). n_e evaluated using Eq. (9), N from SI data [Fig. 8(b)], and l from IF data [Fig. 7(c)] are also plotted (squares). (c) The evaluated plasma size l at each position x.

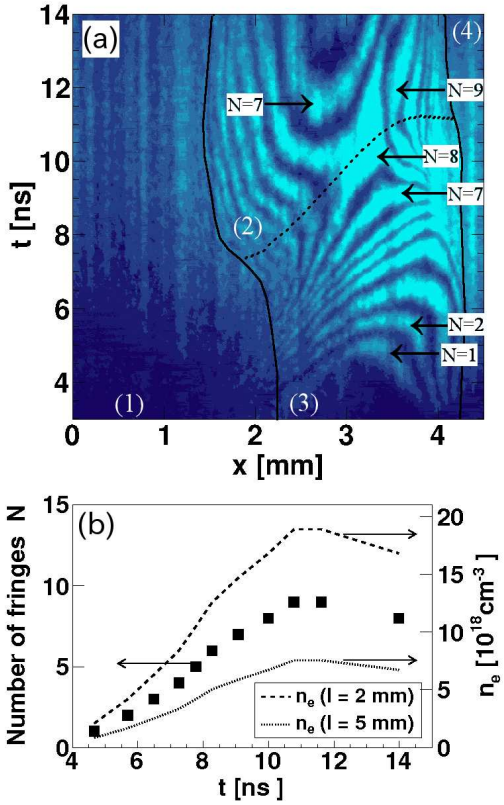

FIG. 8. (color online) (a) The SI data for the double-foil target. As time passes, interference fringes appear through the slit of the streak camera because the plasma density and/or size increase. (b) Temporal variation of the number of fringes N observed at $x = 3.5$ mm (squares in the left y-axis). The evaluated electron densities with $l = 2$ mm (dashed line) and 5 mm (dotted line) are also shown (right y-axis).

at $t = 5$ ns.

Figure 8(a) shows the SI data for the double-foil target. SI observes the interference fringes at $y = 2.6$ mm [dash-dot line in Fig. 7(a)]. Bright areas correspond to the fringes. Figure 8(b) shows the number of fringes N as a function of the emerging time of each fringe at $x = 3.5$ mm. The value N at $t = 10.8$ ns and $t = 11.6$ ns is the same ($N = 9$), and it starts to decrease at $t > 11.6$ ns. N decreases at the time shown with dashed line in Fig. 8(a). Phase difference $\delta\theta$ is expressed with n_e, plasma size l, and N as

$$\delta\theta = 2\pi N \simeq \frac{\omega}{2n_c c} n_e l, \tag{8}$$

where n_c is the critical density for the probe laser, and therefore,

$$n_e\ [\mathrm{cm}^{-3}] \simeq 4.2 \times 10^{18} \times \frac{N}{l\ [\mathrm{mm}]}. \tag{9}$$

It is difficult to calculate the correct electron densities using SI because there is no information about the transverse profiles of the phase difference and, hence, no information on the plasma size l. If we can obtain l, for example from IF, n_e can be calculated from Eq. (9). The evaluated electron densities for $l = 2$ mm (dashed line) and 5 mm (dotted line) are also shown in Fig. 8(b).

Figure 7(c) represents the plasma size l (FWHM) along y-direction evaluated from the interferogram of Fig. 7(a) at $y = 0$–2.6 mm at each x position assuming the axial symmetry. Electron densities evaluated using Eq. (9) with N from the SI data [Fig. 8(b)] and the plasma size l at $t = 5$ ns [Fig. 7(c)] are shown in Fig. 7(b). They are consistent to the values obtained by IF within a factor of two.

However, we can evaluate n_e roughly by SI assuming the plasma size l. The fringes disappeared at the outside of the solid lines [in the regions (1) and (4) in Fig. 8(a)] because the electron density and/or plasma size is large. The detectable electron density is $n_e = (1\text{–}20) \times 10^{18}$ cm^{-3} for IF, and the electron density in the regions (2) and (3) should be less than $\sim 2\times10^{19}$ cm^{-3}. For example, the position of the shock in Fig. 4(b) at $t = 13$ ns is $x = 3.5$ mm, and $N \simeq 8.5$ at the same position and

time as shown in Fig. 8(b). The electron density at the vicinity of the shock derived from Eq. (9) is $n_e \sim 1.8\times10^{19}$ cm^{-3} for $l = 2$ mm and $\sim 7\times10^{18}$ cm^{-3} for $l = 5$ mm. This density is nearly consistent with the estimated values from SI.

D. Collisionality

Before the shock formation, temporal variation of the counter-streaming relative velocity $V(t)$ is estimated as $V(t) = |u_1(t,x) - u_2(t,x)|$, regardless of the position x, where $u_1(t,x) = x/t$ and $u_2(t,x) = -(4.5\text{ mm} - x)/t$ are the flow velocities from the first (left-side) foil and the second (right-side) foil, respectively, and is simply expressed as $V(t) = 4.5\text{ mm}/t$. Using the ion density $n_i = n_e/Z$ for $n_e = 1.7\times10^{19}$ cm^{-3} and $Z = 3.5$, and counter-streaming relative velocity $V(t)$, the ion-ion collision mean-free-path is calculated using the following definition[43]: $\lambda_{ii} = 2\pi\epsilon_0 m_i^2 V^4/(e^4 Z^4 n_i \ln\Lambda)$. In Fig. 4(a), the evaluated λ_{ii} is shown with a solid line to compare with the transition widths. Before the shock formation, λ_{ii} is larger than the transition width by more than an order of magnitude at $t \lesssim 8$ ns, and even after the shock formation, λ_{ii} is larger than shock width, meaning the interaction is nearly collisionless.

IV. CONCLUSION

We have investigated the method of evaluating electron temperatures and densities at the upstream and downstream of a shock produced in nearly collisionless counter-streaming plasmas considering the self-emission intensities and shock conditions. The shock formation was confirmed with the streaked optical pyrometry as a sudden decrease in the transition width. The electron temperatures and densities are evaluated from the measured emission energy combined with the jump condition of the shock. The electron temperature and density jump from $T_0 = 43$ eV and $n_e = 7.4\times10^{18}$ cm^{-3} in the upstream region to $T_1 = 92$ eV and $n_e = 1.7\times10^{19}$ cm^{-3} in the downstream region of the shock. These densities are consistent with that evaluated from streaked interferometry. Interference fringes make complicated structures at $t > 10$ ns and it is impossible to calculate n_e directly from interferometry later in time. Here, the electron density early in time ($t = 5$ ns) was calculated by interferometry, and the temporal variation was observed by streaked interferometry. The ion-ion collision mean-free-path was much larger than the evaluated shock width (< 100 μm) even with the maximum calculable electron density $\sim 1.7\times10^{19}$ cm^{-3}. This technique of inferring electron temperature and density can be applied to shock waves produced in laser-produced plasmas[6,19,21–26,29–33,37–39,44–48] which have been extensively studied with high-power laser systems such as National Ignition Facility (NIF), Omega, and Gekko-XII. This technique can be verified with other diagnostics such as laser Thomson scattering to measure temperature and density directly, and with hydrodynamic and/or particle-in-cell simulations including radiation, plasma–solid interaction, and counter-streaming plasma collision and penetrations.

V. ACKNOWLEDGMENTS

The authors would like to acknowledge the dedicated technical support by the staff at the GEKKO-XII facility for the laser operation and target fabrication. We thank to T. N. Kato for helpful discussions. A part of the experiments was performed under the joint-research project of the Institute of Laser Engineering, Osaka University, and supported by Grant-in-Aid for Scientific Research (B) No. 21340172 and (A) No. 15H02154, by a grant for the Core-to-Core Program from the Japan Society for the Promotion of Science (Project No. 19003), and by a Grant-in-Aid for JSPS Fellows.

[1] F. A. Aharonian, A. G. Akhperjanian, K.-M. Aye, A. R. Bazer-Bachi, M. Beilicke, W. Benbow, D. Berge, P. Berghaus, K. Bernlo, O. Bolz, C. Boisson, C. Borgmeie, F. Breitling, A. M. Brown, J. B. Gordo, P. M. Chadwick, V. R. Chitnis, L.-M. Chounet, R. Cornils, L. Costamante, B. Degrange, A. Djannati-Atai, L. O. Drury, T. Ergin, P. Espigat, F. Feinstein, P. Fleury, G. Fontaine, S. Funk, Y. A. Gallant, B. Giebels, S. Gillessen, P. Goret, J. Guy, C. Hadjichristidis, M. Hauser, G. Heinzelmann, G. Henri, G. Hermann, J. A. Hinton, W. Hofmann, M. Holleran, D. Horns, O. C. de Jager, I. Jung, B. Khelifi, N. Komin, A. Konopelko, I. J. Latham, R. L. Gallou, M. Lemoine, A. Lemiere, N. Leroy, T. Lohse, A. Marcowith, C. Masterson, T. J. L. McComb, M. de Naurois, S. J. Nolan, A. Noutsos, K. J. Orford, J. L. Osborne, M. Ouchrif, M. Panter, G. Pelletier, S. Pita, M. Pohl, G. P. Hlhofer, M. Punch, B. C. Raubenheimer, M. Raue, J. Raux, S. M. Rayner, I. Redondo, A. Reimer, O. Reimer, J. Ripken, M. Rivoal, L. Rob, L. Rolland, G. Rowell, V. Sahakian, L. Sauge, S. Schlenker, R. Schlickeiser, C. Schuster, U. Schwanke, M. Siewert, H. Sol, R. Steenkamp, C. Stegmann, J.-P. Tavernet, C. G. Theoret, M. Tluczykont, D. J. van der Walt, G. Vasileiadis, P. Vincent, B. Visser, H. J. Volk, and S. J. Wagner, Nature **432**, 75 (2004).
[2] Y. Uchiyama, F. A. Aharonian, T. Tanaka, T. Takahashi, and Y. Maeda, Nature **449**, 576 (2007).
[3] A. Bamba, R. Yamazaki, M. Ueno, and K. Koyama, The Astrophysical Journal **589**, 827 (2003).
[4] K. Wenzel, R. Reinhard, T. Sanderson, and E. Sarris, Journal of Geophysical Research **90**, 12 (1985).
[5] E. T. Sarris, G. C. Anagnostopoulos, and S. M. Krimigis, Journal of Geophysical Research **92**, 12083 (1987).
[6] Y. Sakawa, T. Morita, Y. Kuramitsu, and H. Takabe, Advances in Physics: X **1**, 425 (2016).
[7] D. W. Swift, Journal of Geophysical Research **80**, 2096 (1975).
[8] D. W. Swift, Journal of Geophysical Research **81**, 3935 (1976).
[9] F. Mozer, C. Cattell, M. Hudson, R. Lysak, M. Temerin, and R. Torbert, Space Science Reviews **27**, 155 (1980).
[10] D. Melrose and D. B., Australian Journal of Physics **43**, 703 (1990).
[11] T. N. Kato and H. Takabe, Physics of Plasmas **17**, 032114 (2010).
[12] T. N. Kato, The Astrophysical Journal **668**, 974 (2007).
[13] P. Chang, A. Spitkovsky, and J. Arons, The Astrophysical Journal **674**, 378 (2008).
[14] A. Spitkovsky, Astrophysical Journal **673**, L39 (2008), arXiv:0706.3126.

[15]T. N. Kato and H. Takabe, The Astrophysical Journal Letters **681**, 93 (2008).
[16]T. N. Kato and H. Takabe, The Astrophysical Journal **721**, 828 (2010).
[17]F. Fiuza, A. Stockem, E. Boella, R. A. Fonseca, L. O. Silva, D. Haberberger, S. Tochitsky, C. Gong, W. B. Mori, and C. Joshi, Physical Review Letters **109**, 215001 (2012).
[18]B. Remington, R. Drake, and D. Ryutov, Reviews of Modern Physics **78**, 755 (2006).
[19]Y. Sakawa, T. Ide, T. Morita, K. Tomita, K. Uchino, Y. Kuramitsu, N. Ohnishi, and H. Takabe, High Energy Density Physics , accepted (2017).
[20]H. Takabe, T. N. Kato, Y. Sakawa, Y. Kuramitsu, T. Morita, T. Kadono, K. Shigemori, K. Otani, H. Nagatomo, T. Norimatsu, S. Dono, T. Endo, K. Miyanishi, T. Kimura, A. Shiroshita, N. Ozaki, R. Kodama, S. Fujioka, H. Nishimura, D. Salzman, B. Loupias, C. Gregory, M. Koenig, J. N. Waugh, N. C. Woolsey, D. Kato, Y.-T. Li, Q.-L. Dong, S.-J. Wang, Y. Zhang, J. Zhao, F.-L. Wang, H.-G. Wei, J.-R. Shi, G. Zhao, J.-Y. Zhang, T.-S. Wen, W.-H. Zhang, X. Hu, S.-Y. Liu, Y. K. Ding, L. Zhang, Y.-J. Tang, B.-H. Zhang, Z.-J. Zheng, and Z.-M. Sheng, Plasma Physics and Controlled Fusion **50**, 124057 (2008).
[21]A. R. Bell, P. Choi, A. E. Dangor, O. Willi, D. A. Bassett, and C. J. Hooker, Physical Review A **38**, 1363 (1988).
[22]P. M. Nilson, S. P. D. Mangles, L. Willingale, M. C. Kaluza, a. G. R. Thomas, M. Tatarakis, Z. Najmudin, R. J. Clarke, K. L. Lancaster, S. Karsch, J. Schreiber, R. G. Evans, a. E. Dangor, and K. Krushelnick, Physical Review Letters **103**, 255001 (2009).
[23]T. Morita, Y. Sakawa, Y. Kuramitsu, S. Dono, H. Aoki, H. Tanji, T. N. Kato, Y. T. Li, Y. Zhang, X. Liu, J. Y. Zhong, H. Takabe, and J. Zhang, Physics of Plasmas **17**, 122702 (2010).
[24]Y. Kuramitsu, Y. Sakawa, T. Morita, C. Gregory, J. Waugh, S. Dono, H. Aoki, H. Tanji, M. Koenig, N. Woolsey, and H. Takabe, Physical Review Letters **106**, 175002 (2011).
[25]L. Romagnani, S. Bulanov, M. Borghesi, P. Audebert, J. Gauthier, K. Löwenbrück, A. Mackinnon, P. Patel, G. Pretzler, T. Toncian, and O. Willi, Physical Review Letters **101**, 025004 (2008).
[26]T. Morita, N. L. Kugland, W. Wan, R. Crowston, R. P. Drake, F. Fiuza, G. Gregori, C. Huntington, T. Ishikawa, M. Koenig, C. Kuranz, M. C. Levy, D. Martinez, J. Meinecke, F. Miniati, C. D. Murphy, A. Pelka, C. Plechaty, R. Presura, N. Quirós, B. A. Remington, B. Reville, J. S. Ross, D. D. Ryutov, Y. Sakawa, L. Steele, H. Takabe, Y. Yamaura, N. Woolsey, and H.-S. Park, Journal of Physics: Conference Series **688**, 012071 (2016).
[27]R. P. Drake and G. Gregori, The Astrophysical Journal **749**, 171 (2012).
[28]D. D. Ryutov, N. L. Kugland, H. S. Park, C. Plechaty, B. A. Remington, and J. S. Ross, Plasma Physics and Controlled Fusion **54**, 105021 (2012).
[29]J. S. Ross, S. H. Glenzer, P. Amendt, R. Berger, L. Divol, N. L. Kugland, O. L. Landen, C. Plechaty, B. Remington, D. Ryutov, W. Rozmus, D. H. Froula, G. Fiksel, C. Sorce, Y. Kuramitsu, T. Morita, Y. Sakawa, H. Takabe, R. P. Drake, M. Grosskopf, C. Kuranz, G. Gregori, J. Meinecke, C. D. Murphy, M. Koenig, A. Pelka, A. Ravasio, T. Vinci, E. Liang, R. Presura, A. Spitkovsky, F. Miniati, and H.-S. Park, Physics of Plasmas **19**, 056501 (2012).
[30]H.-S. Park, D. Ryutov, J. Ross, N. Kugland, S. Glenzer, C. Plechaty, S. Pollaine, B. Remington, A. Spitkovsky, L. Gargate, G. Gregori, A. Bell, C. Murphy, Y. Sakawa, Y. Kuramitsu, T. Morita, H. Takabe, D. Froula, G. Fiksel, F. Miniati, M. Koenig, A. Ravasio, A. Pelka, E. Liang, N. Woolsey, C. Kuranz, R. Drake, and M. Grosskopf, High Energy Density Physics **8**, 38 (2012).
[31]W. Fox, G. Fiksel, a. Bhattacharjee, P.-Y. Chang, K. Germaschewski, S. X. Hu, and P. M. Nilson, Physical Review Letters **111**, 225002 (2013).
[32]C. M. Huntington, F. Fiuza, J. S. Ross, A. B. Zylstra, R. P. Drake, D. H. Froula, G. Gregori, N. L. Kugland, C. C. Kuranz, M. C. Levy, C. K. Li, J. Meinecke, T. Morita, R. Petrasso, C. Plechaty, B. A. Remington, D. D. Ryutov, Y. Sakawa, A. Spitkovsky, H. Takabe, and H.-S. Park, Nat Phys **11**, 173 (2015).
[33]T. Morita, Y. Sakawa, K. Tomita, T. Ide, Y. Kuramitsu, K. Nishio, K. Nakayama, K. Inoue, T. Moritaka, H. Ide, M. Kuwada, K. Tsubouchi, K. Uchino, and H. Takabe, Physics of Plasmas **20**, 092115 (2013).
[34]R. L. Kauffman, H. N. Kornblum, D. W. Phillion, C. B. Darrow, B. F. Lasinski, L. J. Suter, a. R. Theissen, R. J. Wallace, and F. Ze, Review of Scientific Instruments **66**, 678 (1995).
[35]J. E. Miller, T. R. Boehly, a. Melchior, D. D. Meyerhofer, P. M. Celliers, J. H. Eggert, D. G. Hicks, C. M. Sorce, J. a. Oertel, and P. M. Emmel, The Review of scientific instruments **78**, 034903 (2007).
[36]R. P. Drake, D. W. Phillion, K. Estabrook, R. E. Turner, R. L. Kauffman, and E. M. Campbell, Physics of Fluids B: Plasma Physics **1**, 1089 (1989).
[37]Y. Kuramitsu, Y. Sakawa, J. N. Waugh, C. D. Gregory, T. Morita, S. Dono, H. Aoki, H. Tanji, B. Loupias, M. Koenig, N. Woolsey, and H. Takabe, The Astrophysical Journal **707**, L137 (2009).
[38]J. S. Ross, D. P. Higginson, D. Ryutov, F. Fiuza, R. Hatarik, C. M. Huntington, D. H. Kalantar, A. Link, B. B. Pollock, B. A. Remington, H. G. Rinderknecht, G. F. Swadling, D. P. Turnbull, S. Weber, S. Wilks, D. H. Froula, M. J. Rosenberg, T. Morita, Y. Sakawa, H. Takabe, R. P. Drake, C. Kuranz, G. Gregori, J. Meinecke, M. C. Levy, M. Koenig, A. Spitkovsky, R. D. Petrasso, C. K. Li, H. Sio, B. Lahmann, A. B. Zylstra, and H.-S. Park, Physical Review Letters **118**, 185003 (2017).
[39]T. Morita, Y. Sakawa, Y. Kuramitsu, S. Dono, T. Ide, S. Shibata, H. Aoki, H. Tanji, T. Sano, A. Shiroshita, J. N. Waugh, C. D. Gregory, N. C. Woolsey, and H. Takabe, The Review of scientific instruments **83**, 10D514 (2012).
[40]T. Ide, Y. Sakawa, Y. Kuramitsu, T. Morita, H. Tanji, K. Nishio, T. N. Kato, N. Ohnishi, C. D. Gregory, N. Woolsey, A. Diziere, M. Koenig, S. Wang, and Q. Dong, Plasma Fusion Res. **6**, 2404057 (2011).
[41]G. B. Rybicki and A. P. Lightman, *Radiative Processes in Astrophysics* (Wiley-VCH, 1985) p. 400.
[42]W. Karzas and R. Latter, The Astrophysical Journal Supplement Series **6**, 167 (1961).
[43]L. Spitzer, *Physics of Fully Ionized Gases*, 2nd ed. (Interscience, 1962).
[44]C. Courtois, R. a. D. Grundy, a. D. Ash, D. M. Chambers, N. C. Woolsey, R. O. Dendy, and K. G. McClements, Physics of Plasmas **11**, 3386 (2004).
[45]N. C. Woolsey, C. Courtois, and R. O. Dendy, Plasma Physics and Controlled Fusion **46**, B397 (2004).
[46]N. L. Kugland, D. D. Ryutov, P.-Y. Chang, R. P. Drake, G. Fiksel, D. H. Froula, S. H. Glenzer, G. Gregori, M. Grosskopf, M. Koenig, Y. Kuramitsu, C. Kuranz, M. C. Levy, E. Liang, J. Meinecke, F. Miniati, T. Morita, A. Pelka, C. Plechaty, R. Presura, A. Ravasio, B. A. Remington, B. Reville, J. S. Ross, Y. Sakawa, A. Spitkovsky, H. Takabe, and H.-S. Park, Nature Physics **8**, 809 (2012).
[47]Y. Kuramitsu, Y. Sakawa, S. Dono, C. Gregory, S. Pikuz, B. Loupias, M. Koenig, J. Waugh, N. Woolsey, T. Morita, T. Moritaka, T. Sano, Y. Matsumoto, A. Mizuta, N. Ohnishi, and H. Takabe, Physical Review Letters **108**, 195004 (2012).
[48]H.-S. Park, C. M. Huntington, F. Fiuza, R. P. Drake, D. H. Froula, G. Gregori, M. Koenig, N. L. Kugland, C. C. Kuranz, D. Q. Lamb, M. C. Levy, C. K. Li, J. Meinecke, T. Morita, R. D. Petrasso, B. B. Pollock, B. A. Remington, H. G. Rinderknecht, M. Rosenberg, J. S. Ross, D. D. Ryutov, Y. Sakawa, A. Spitkovsky, H. Takabe, D. P. Turnbull, P. Tzeferacos, S. V. Weber, and A. B. Zylstra, Physics of Plasmas **22**, 056311 (2015).